Research on Fluctuation External Disturbance Suppression of Permanent Magnetic Levitation Platform

Wenzhe PEI*, Chuan ZHAO*, Feng SUN*, Junjie JIN*, Ran ZHOU*, Xiaoyou ZHANG**,*** and Huachun WU
*School of Mechanical Engineering, Shenyang University of Technology
No.111, Shenliao West Road, Economic and Technological Development Zone, Shenyang 110870, China
E-mail: Zhaochuan@sut.edu.cn
**Department of Mechanical Engineering, Nippon Institute of Technology
4-1 Gakuendai, Miyashiro-machi, Minamisaitama-gun, Saitama 345-8501, Japan
***School of Mechanical and Electronic Engineering, Wuhan University of Technology
No.122, Luoshi Road, Wuhan, Hubei, China

Abstract

In this paper, a permanent magnet levitation platform with variable flux path mechanism for ultra-clean transport scenarios is presented, and a fractional-order PID centralized control strategy is designed to suppress fluctuating external disturbances. Firstly, the mechanisms of variable flux path and magnetic force regulation are introduced, and the four units support configuration, measurement scheme and feedback control principle of the levitation platform are explained. Then, the mathematical model of the levitation platform is established, and a centralized control strategy along with the fractional-order PID algorithm is designed to achieve stable levitation in three degrees of freedom. Subsequently, experiments are conducted to evaluate the stable levitation performance of the system, including initiation levitation and dynamic response to load variations. The experimental results demonstrate that the fractional-order PID centralized controller achieves smooth start-up with reduced overshoot, superior robustness under mass loading/unloading.

Finally, the sinusoidal current is applied to the electromagnetic coil to generate vertically fluctuating disturbance force, simulating linear motor-induced disturbances acting on the levitation platform. Under fluctuating disturbance conditions, the fractional-order PID controlled levitation platform exhibited rapid suppression of air gap fluctuations and significantly reduced vibration amplitudes across all degrees of freedom. Compared with standard PID, the fractional-order PID controller achieved faster stabilization without residual oscillations, maintaining smoother pitch and roll responses. These results highlight the superior capability of fractional-order PID centralized control strategy in attenuating low-frequency fluctuating external disturbances and preserving platform stability.

Keywords: Magnetic levitation, Fluctuation External Disturbance, fractional-order PID, permanent magnet, variable flux path mechanism

1. Introduction

Magnetic levitation technology enables support or actuation without mechanical contact. Driven by modern advancements in mechatronics, both theoretical and applied aspects of magnetic levitation have witnessed marked progress. Benefiting from contactless operation that allows for high-speed and lubrication-free operation, magnetic levitation has become a prevalent area of application and research. High-speed maglev trains have exceeded 600 km/h in experimental trials (Feng et al., 2025), while medium-speed maglev trains are favored in urban transit for their low-noise feature (Hu et al., 2024). For magnetic bearings, they support high-speed motors to reach extreme performance (Wu et al., 2021; Maslen and Schweitzer, 2009), while ensuring reliability in critical equipment such as artificial organs (Xu et al., 2025).

Furthermore, owing to its contactless operation, magnetic levitation can effectively eliminate particle generation caused by mechanical wear. This advantage makes magnetic levitation-based dust-free automation systems particularly suitable for deployment in ultra-clean environments, such as those found in semiconductor fabrication facilities. Zhou et al. proposed a magnetic levitation transport system in which electromagnetic coils are employed for levitation and

guidance control, while a linear motor is utilized to achieve long-stroke translational motion (Duan et al., 2011). In addition, a fuzzy decoupling strategy was proposed, and the results demonstrated a significant reduction in the coupling between degrees of freedom (DOF) (Zhou et al., 2018). Kim et al. introduced a high-precision pallet-type maglev transport system, in which dead-zone control was specifically addressed. The system demonstrated stable and accurate performance in long-duration experiments (Ha et al., 2018; Kim et al., 2020). A bearingless slice hysteresis motor was developed by Zhou et al. for transport applications in ultra-clean vacuum environments. In this system, guidance is actively controlled by electromagnetic coils, while levitation is passively achieved through reluctance stiffness (Zhou and Trumper, 2021).

With the advancement of second-generation rare-earth permanent magnetic materials, the performance of permanent magnets (PM) has improved significantly. Integrating PM into the magnetic circuit can effectively reduce the power consumption of magnetic levitation systems, potentially achieving near-zero energy operation (Kim et al., 2024; Zhao et al., 2022a). A 3D multibody dynamic model of an EM-PM hybrid magnetically levitated conveyor is developed to investigate its vibration behavior and the effectiveness of a secondary suspension system in mitigating the dynamic interaction between the conveyor and the rail (Kim et al., 2013). A permanent maglev system with a variable flux path mechanism was proposed by Sun et al., in which a servo actuator is used to rotate cylindrical dipole PM diametral magnetized, enabling controllable magnetic force and stable levitation (Sun et al., 2010; Zhao et al., 2022b). This system exhibits quasi-zero power consumption and can maintain low energy usage even under variations in load or air-gap length (Zhao et al., 2020). Therefore, a permanent maglev platform composed of four variable flux path units was proposed, and a control strategy was designed to achieve stable levitation and motion control (Sun et al., 2022).

Nevertheless, the limited bandwidth of the servo actuator responsible for adjusting the PM angle, substantially lower than that of typical maglev systems, restricts the platforms robustness, making the control system susceptible to divergence under external disturbances. Therefore, to integrate with linear motors for ultra-clean transport applications, it is necessary to investigate fluctuation disturbance rejection methods to mitigate the adverse effects of normal force fluctuations from the linear motor on levitation stability. Researchers have extensively explored active disturbance suppression methods for magnetic levitation systems, including standard PID control, modern optimal and robust control techniques, as well as advanced approaches such as fuzzy control (Song et al., 2015; Wu et al., 2025). Among these, fractional-order PID (FOPID) control has emerged as a prominent research focus due to its unique memory effect and flexible dynamic characteristics, enabling effective maintaining magnetic levitation system stability (Chopade et al., 2018; Swethamarai and Lakshmi, 2022; Wang et al., 2025).

In this study, the disturbance suppression problem of a permanent magnet levitation platform is investigated using a fractional-order PID control strategy. First, the working principle of the levitation platform is introduced, and its mathematical model is established. Then, a centralized control strategy employing FOPID is then developed to enhance levitation stability and dynamic behavior. To evaluate its effectiveness, initiation levitation experiment and mass loading variation experiment are performed. Finally, a sinusoidal current is applied to the coil to simulate the vertical fluctuation forces typically generated by linear motors. Corresponding fluctuation disturbance suppression experiments are performed, and the response performance is compared with the standard PID.

2. System description and mathematical model

2.1. Variable flux path mechanism

The variable flux path is a type of magnetic force regulation method achieved by adjusting the magnetic configuration within magnetic units. As illustrated in Fig. 1, this variable flux path magnetic unit is composed of two F-type ferromagnetic cores and a cylindrical dipole-type PM that is magnetized in the diametral direction. In this study, the PM angle is defined to be 0◦ when the magnetization direction of the PM is aligned vertically upward. In this case, the magnetic flux emanates from the north pole of the permanent magnet, passes through the two F-type iron cores, and returns to the south pole, forming a closed flux path. Except for minor magnetic leakage, almost no magnetic flux passes through the air gaps and the iron rail. As a result, provided that the air gap length is not excessively small, the magnetic force between the magnetic unit and the iron rail can be neglected. If it is equated to the typical electromagnetic levitation system, the 0◦ PM angle can be equated to 0A excitation current of typical electromagnetic levitation system. If analogies are considered, the 0◦ PM angle of this system can be regarded as equivalent to the 0A excitation current in a typical electromagnetic levitation system.

Then, the permanent magnet rotates clockwise under the actuation of the servo motor. A portion of the magnetic

flux passes through the F-type iron cores, the air gaps, and the iron rail forms a closed flux path, while the remaining flux returns directly through the F-type cores to the opposite pole. As shown in Fig. 1, a larger proportion of the magnetic flux passes through the air gap as the PM angle increases. Consequently, the magnetic density of air gap increases progressively as the PM angle increases. This indicates that the magnetic energy stored in the air gap increases, based on the principle of virtual work, resulting in a corresponding increase in magnetic force. When the permanent magnet angle reaches 90◦, the magnetic flux density in the air gap and the resulting magnetic force reaches their maximum value. Under this condition, the entire magnetic flux produced by the PM, excluding a small portion of leakage flux, is directed through the levitation air gap. As the PM angle continues to increase beyond 90◦, the air gap magnetic density begins to decline, and therefore, this range is generally not utilized in levitation control scenarios.

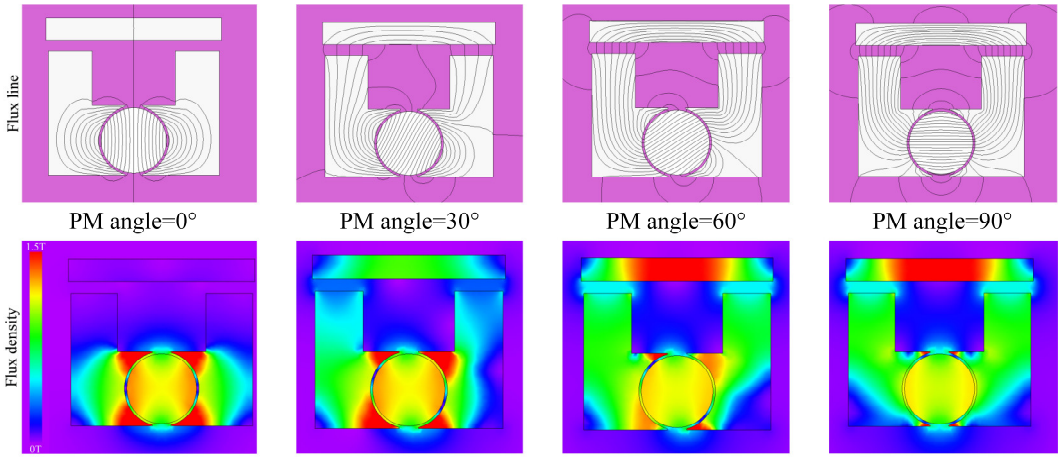

Fig.1 Principle of Variable flux path

2.2. Structure of permanent maglev platform

As described in Section 2.1, a single variable flux path magnetic unit can achieve active magnetic force control by adjusting the PM angle. Accordingly, three such controlled magnetic units are sufficient to achieve 3-DOF feedback control of the platform. To enhance stability and ensure even load sharing, the platform utilizes four magnetic units. As shown in Fig. 2, the levitation platform prototype consists of three main parts. The first component includes the supporting frame and the iron rail, which is designed to be extendable along the motion direction of the linear motor to accommodate long-distance transport.

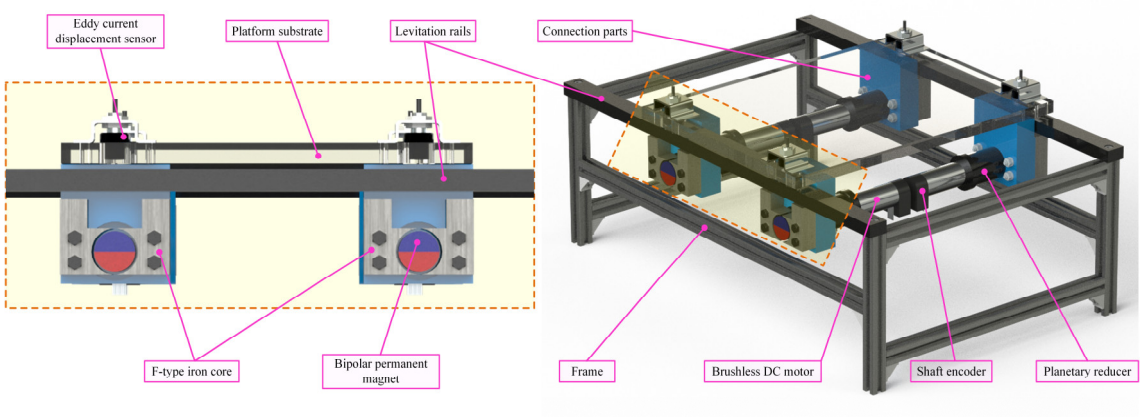

Fig. 2 structure of maglev platform

The second part consists of the platform substrate and four eddy current displacement sensors, which are positioned directly above the magnetic units. These sensors indirectly measure the levitation air gap lengths in real time by detecting the distances between the substrate and the iron rail above magnetic units. The third part consists of four variable flux path magnetic units, each comprising a servo rotary actuator, a permanent magnet, and two F-type iron cores. And each actuator is composed of a brushless DC motor, a planetary reducer, an encoder, and a servo driver. It is also noted that the lateral translation and yaw angle of the levitation platform are passively controlled. Due to the characteristics of

magnetic reluctance, when a magnetic unit deviates from the iron rail, an equivalent positive stiffness is generated, which tends to restore it to its original position.

2.3. Mathematical model

The dynamic analysis of the levitation platform is carried out, and a schematic diagram is shown in Fig. 3. The relationships between forces and displacements in the 3-DOF are obtained, as presented in Equ.1. Subsequently, experimental measurements of the magnetic force at various PM angles and air-gap lengths are illustrated in Fig. 4. This observation confirms the nonlinear nature of the magnetic force. The magnetic force generated by a magnetic unit can be expressed as shown in Equ.2 (Zhao et al., 2020). It can be observed that the magnetic force is proportional to the square of the sine of the magnet angle and inversely proportional to the square of the air gap length.

$$\begin{cases} m\ddot{z} = F_1 + F_2 + F_3 + F_4 - mg - c_z\dot{z} \\ J_\gamma\ddot{\gamma} = (-F_1 - F_2 + F_3 + F_4)\cdot e - c_\gamma\dot{\gamma} \\ J_\zeta\ddot{\zeta} = (-F_1 + F_2 + F_3 - F_4)\cdot e - c_\zeta\dot{\zeta} \end{cases} \tag{1}$$

Where, the variables z, γ, and ζ denote the vertical displacement, pitch angle, and roll angle of the platform, respectively. $\sigma_i(i=1,2,3,4)$ represent the displacements of the four magnetic units, respectively. m, J_γ and J_ζ represent the mass and the moments of inertia of the platform about the corresponding axes. $F_i(i=1,2,3,4)$ denotes the magnetic force generated by each magnetic unit. c_z, c_γ and c_ζ represent the damping coefficients along the three axes, which can be considered negligible for the maglev platform.

$$F_m = k_m \frac{\sin^2\theta}{(d+\Delta d_f)} \tag{2}$$

Where, F_m denotes the magnetic force generated by magnetic unit, and k_m is the magnetic force coefficient. θ is the PM angle, d is the levitation air-gap length, and Δd_f is the leakage flux compensation constant.

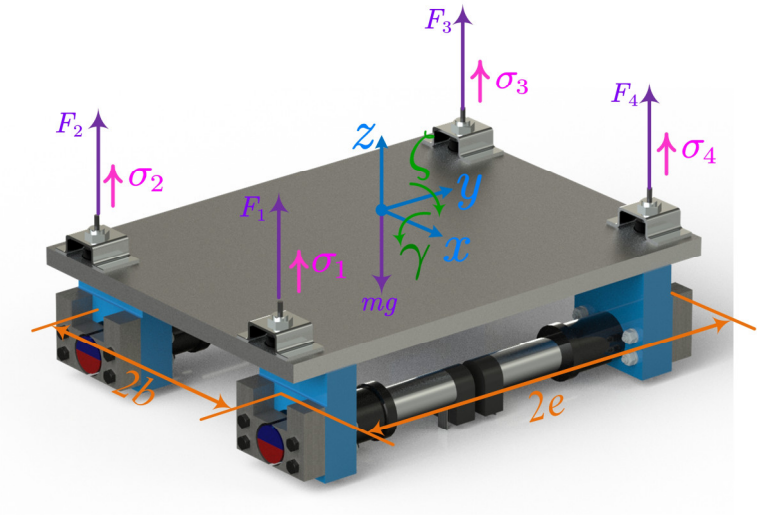

Fig. 3 Dynamic analysis of maglev platform

At steady state, the magnetic force generated of each unit at the operating point (d_0,θ_0) is given by Equ.3. By applying a Taylor series expansion around the operating point (d_0,θ_0) and neglecting higher-order terms, the magnetic force can be linearized, resulting in the linear expression shown in Equ.4. Assuming the upward direction as positive, the displacement σ_i of the magnetic unit is related to the air-gap variation by $\sigma_i = d_0 - d_i$. Meanwhile, defining the change of the PM angle as $\vartheta_i = \theta_i - \theta_0$ leads to the formulation given in Equ.5. Equation.1, Equ.3, and Equ.5 are combined and reformulated into a matrix representation, resulting in the linearized dynamic model of the levitation platform presented in Equ.6.

$$F_0 = \frac{1}{4}mg \tag{3}$$

$$F_i = F_0 + \frac{\partial F_m}{\partial d}\cdot(d_i - d_0) + \frac{\partial F_m}{\partial \theta}\cdot(\theta_i - \theta_0), (i = 1, 2, 3, 4) \tag{4}$$

$$F_i = F_0 + \frac{-\partial F_m}{\partial d}\cdot\sigma_i + \frac{\partial F_m}{\partial \theta}\cdot\vartheta_i, (i = 1, 2, 3, 4) \tag{5}$$

$$\begin{bmatrix} m & & \\ & J_\gamma & \\ & & J_\zeta \end{bmatrix}\begin{bmatrix} \ddot{z} \\ \ddot{\gamma} \\ \ddot{\zeta} \end{bmatrix} = \frac{-\partial F_m}{\partial d}\mathbf{N}_1\begin{bmatrix} \sigma_1 \\ \sigma_2 \\ \sigma_3 \\ \sigma_4 \end{bmatrix} + \frac{\partial F_m}{\partial \theta}\mathbf{N}_1\begin{bmatrix} \vartheta_1 \\ \vartheta_2 \\ \vartheta_3 \\ \vartheta_4 \end{bmatrix} - \begin{bmatrix} c_z & & \\ & c_\gamma & \\ & & c_\zeta \end{bmatrix}\begin{bmatrix} \dot{z} \\ \dot{\gamma} \\ \dot{\zeta} \end{bmatrix} \tag{6}$$

Here, $\mathbf{N}_1 = \begin{bmatrix} 1 & 1 & 1 & 1 \\ -e & -e & e & e \\ -b & b & b & -b \end{bmatrix}$ denotes the system matrix.

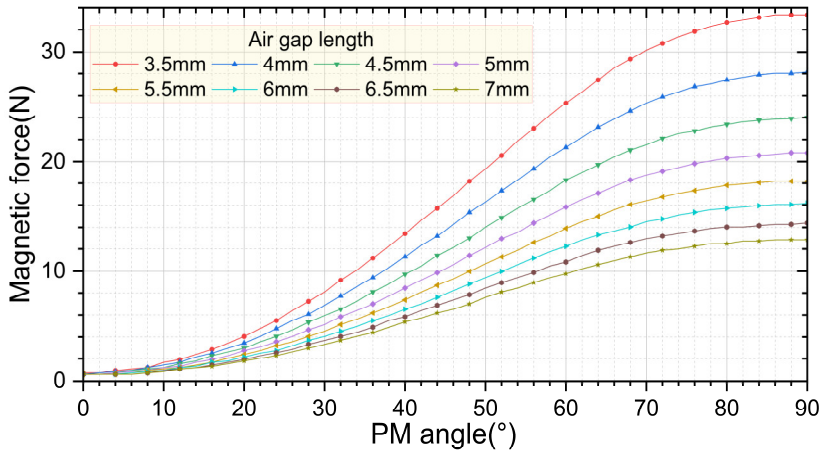

Fig. 4 Magnetic force of variable flux path unit

Furthermore, the transformation between the displacements of the four magnetic units and the 3-DOF of platform is determined, as presented in Equ.7 and Equ.8. By combining Equ.6. and Equ.7, the dynamic model of the maglev platform can be obtained, as shown in Equ.8.

$$[\sigma_1 \quad \sigma_2 \quad \sigma_3 \quad \sigma_4]^{\mathrm{T}} = \mathbf{N}_2[z \quad \gamma \quad \zeta]^{\mathrm{T}} \tag{7}$$

$$\begin{bmatrix} m & & \\ & J_\gamma & \\ & & J_\zeta \end{bmatrix}\begin{bmatrix} \ddot{z} \\ \ddot{\gamma} \\ \ddot{\zeta} \end{bmatrix} = \frac{-\partial F_m}{\partial d}\mathbf{N}_1\mathbf{N}_2\begin{bmatrix} z \\ \gamma \\ \zeta \end{bmatrix} + \frac{\partial F_m}{\partial \theta}\mathbf{N}_1\begin{bmatrix} \vartheta_1 \\ \vartheta_2 \\ \vartheta_3 \\ \vartheta_4 \end{bmatrix} - \begin{bmatrix} c_z & & \\ & c_\gamma & \\ & & c_\zeta \end{bmatrix}\begin{bmatrix} \dot{z} \\ \dot{\gamma} \\ \dot{\zeta} \end{bmatrix} \tag{8}$$

Here, $\mathbf{N}_2 = \mathbf{N}_1^{\mathrm{T}} = \begin{bmatrix} 1 & -e & -b \\ 1 & -e & b \\ 1 & e & b \\ 1 & e & -b \end{bmatrix}$ is the coordinate transformation matrix.

3. Feedback control strategy design

3.1. Centralized control strategy

For the permanent magnet levitation platform, two control strategies can be applied to achieve stable levitation. The first strategy is a decentralized control approach, in which each of the four magnetic units independently regulates its own air-gap length through feedback control. In contrast, the second strategy employs centralized sensing and control,

whereby the feedback controller directly regulates the platform's 3-DOF based on integrated measurements. In comparison with decentralized control, centralized control offers the advantage of reduced coupling among the system's control channels. In order to realize effective motion control and ensure better system stability, centralized control should be implemented.

To implement centralized control, an integrated measurement method must first be established. As shown in Equ.9, in the practical system, the matrix $\mathbf{N}_3$ is used to convert the measured displacements of individual magnetic units into the corresponding degrees of freedom of the platform. Secondly, the output of the 3-DOF feedback controller should be allocated to the four magnetic units. As indicated in Equ.5, to maintain the operating magnetic force, the control relationship between the PM angle and the air gap length can be approximated as linear near the operating point. Therefore, the allocation rule from the 3-DOF control outputs to four PM angles is given in Equ.10.

$$[z \quad \gamma \quad \zeta]^{\mathrm{T}} = \mathbf{N}_3 [\sigma_1 \quad \sigma_2 \quad \sigma_3 \quad \sigma_4]^{\mathrm{T}} \tag{9}$$

$$[\vartheta_1 \quad \vartheta_2 \quad \vartheta_3 \quad \vartheta_4]^{\mathrm{T}} = \mathbf{N}_2 [\vartheta_z \quad \vartheta_\gamma \quad \vartheta_\zeta]^{\mathrm{T}} \tag{10}$$

Here, $\mathbf{N}_3 = \begin{bmatrix} 1 & 1 & 1 & 1 \\ -1/e & -1/e & 1/e & 1/e \\ -1/b & 1/b & 1/b & -1/b \end{bmatrix}$ is the pseudoinverse of $\mathbf{N}_2$.

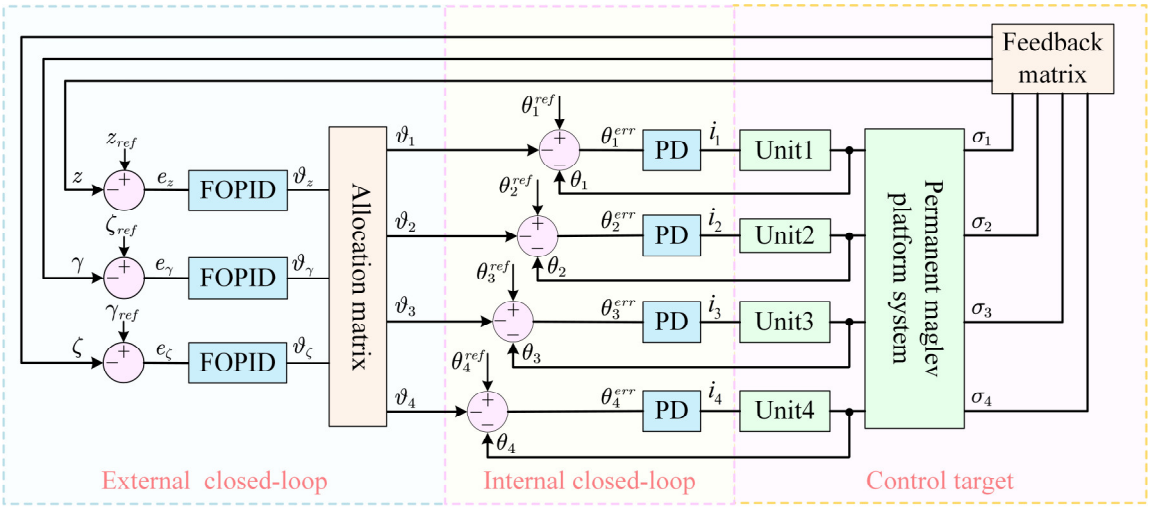

Fig. 5 Controller configuration for levitation platform

As illustrated in Fig. 5, the control configuration of the levitation platform consists of an internal closed-loop and a external closed-loop. The internal closed-loop is responsible for regulating the PM angles through servo actuators with PD control, ensuring high dynamic response. For the external closed-loop, its primary function is achieve 3-DOF motion control in vertical displacement z, pitch angle ζ, and roll angle γ. The 3-DOF controller generates equivalent compensation angles, which are then allocated to the four magnetic units using an allocation matrix. By combining the compensation angles with the steady-state angles at the operating point, the reference angles for each magnetic unit are obtained and transmitted to the inner loop for precise actuator control, thereby enabling the system to respond effectively to platform displacement and orientation deviations.

3.2. Fractional-order PID control

To enhance the disturbance rejection and robustness of the platform, fractional-order PID controllers are employed in the external closed-loop. As shown in Fig. 5, each DOF is controlled by an individual FOPID controller that generates a corresponding compensation signal ϑ_z, ϑ_γ, or ϑ_ζ. The structure of the FOPID controller is illustrated in Fig. 6(a) and Equ. 11, the FOPID controller introduces two additional tuning parameters: the integral order and the derivative order. This generalization leverages the unique properties of fractional calculus, particularly its memory effect and tunable dynamic response.

$$\vartheta_j(t) = K_P^j e_j(t) + K_I^j D_t^{-\lambda_j} e_j(t) + K_D^j D_t^{\mu_j} e_j(t), \quad j = z, \gamma, \zeta \tag{11}$$

Where, $\vartheta_j(t)$ is control output, $e_j(t)$ is feedback error. The K_P^j, K_I^j and K_D^j are proportional gain, integral gain and differential gain respectively. The $\lambda_j (0 < \lambda_j < 1)$ is the integral order, and the $\mu_j (0 < \mu_j < 1)$ is the derivative order.

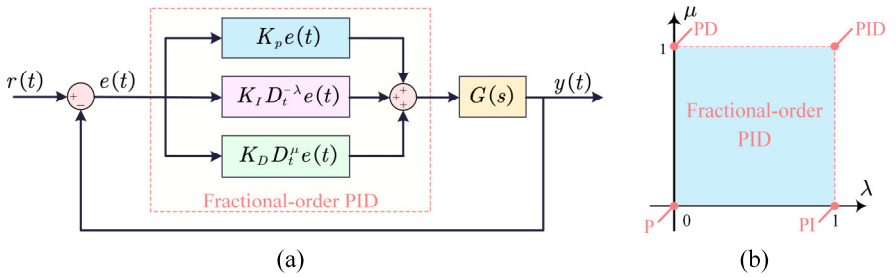

(a) (b)

Fig. 6 Diagram of fractional order PID

As shown in Fig. 6(b), the FOPID is represented by the square region, whose four boundaries are P, PD, PID and PI, respectively. The fractional integral and derivative operators introduce long-term memory into the control law, allowing the system to account for historical error trends rather than just instantaneous deviations. This results in stronger suppression of low-frequency or persistent disturbances. In addition, two additional tuning parameters, which are integrated order λ and derivative order μ, allow for more flexible frequency response shaping. By adjusting two orders, the low-frequency gain in the Bode plot can be increased for better steady-state performance while mitigating phase lag. Furthermore, the high-frequency gain is also potentially reduced to suppress noise of measurement signal. Such flexibility cannot be provided by integer-order PID.

4. Stable levitation Experiment and analysis

4.1. Prototype and experimental system

As illustrated in Fig. 7, real-time control and data acquisition in the experiments is implemented using the dSPACE rapid prototyping system. The control algorithm is developed within the MATLAB/Simulink environment and deployed via the dSPACE interface, enabling efficient automatic code generation and seamless integration with the hardware components. The dSPACE interface performs measurement and feedback control through analog signal interfaces and encoder counters, operating at a sampling frequency of 1 kHz. Specifically, in external closed-loop control, the analog displacement signals from the sensors are sampled and processed by the dSPACE system. The resulting control commands are then transmitted to the servo amplifiers in analog form. As for external closed-loop control, incremental encoders are employed to measure and provide feedback on the PM angles driven by the servo motors.

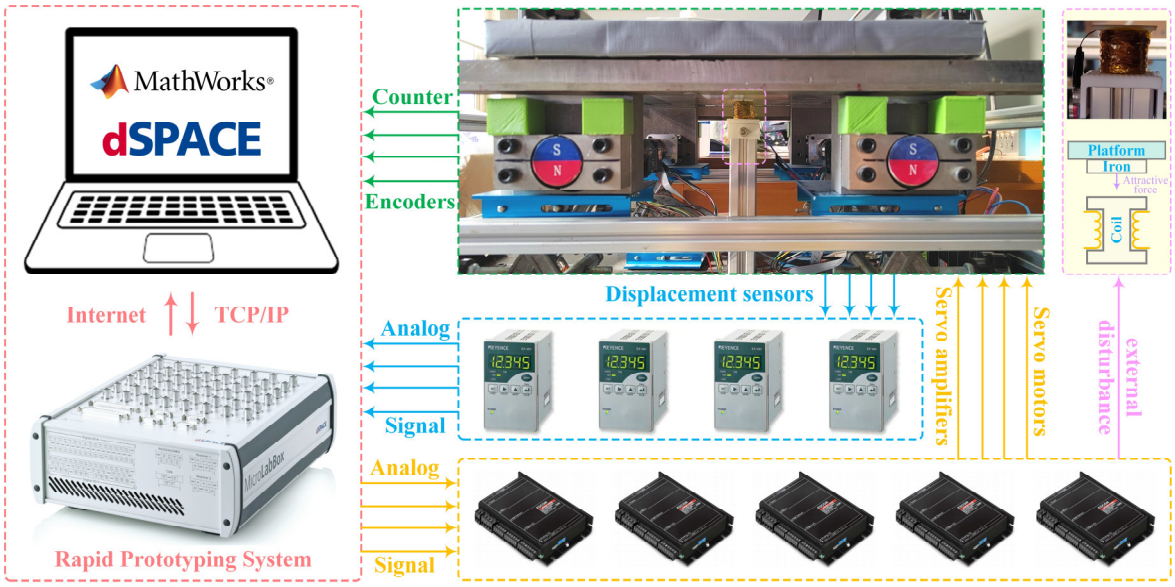

Fig. 7 Diagram of prototype and experimental system

Each of the four magnetic units is actuated by a servo motor, which consists of a brushless DC motor, a planetary gearbox, and an incremental encoder. The brushless DC motor is a Maxon EC-max 30 with 60-watt rate power, paired with a planetary gearbox with a ratio of 30:1. And the motor shaft is equipped with a 500 count/r incremental encoder (HEDL 5540). Also, the four-quadrant servo amplifiers (ESCON 70/10) are used to drive the motors, configured to operate in current control mode with a rated output current of 10 A, a maximum bus voltage of 70 V, and a PWM carrier frequency of 53.6 kHz. Additionally, four eddy current displacement sensors (Keyence EX-422V), each with a 10 mm measuring range, 2 μm resolution, and a maximum sampling rate of 40,000 samples/s, are embedded in the maglev platform to indirectly measure the levitation air gaps. To apply external disturbances, the dSPACE system outputs control signals to a servo amplifier (ESCON 70/10), which drives an electromagnetic coil to produce a vertically attractive force acting on the maglev platform.

4.2. Initiation levitation experiment

To verify the centralized FOPID control strategy proposed in Section 3, the levitation experiments are implemented with the experimental system described in Section 4.1. Firstly, the initiation levitation experiment is executed. As shown in Fig. 8(a), the levitation enable signal is issued at 0.5 s. As shown in Fig. 8(b), once the enable signal is applied, the control current rapidly rises to its saturation limit. Under the excitation of the control current, the servo motors are rapidly activated, and the PM angles respond promptly. Consequently, as the magnetic forces produced by the units increase, the attractive force overcomes gravity, and the air gap reduces from its initial 5 mm. After approximately 1 second, the air gaps of the four magnetic units reach a dynamically stable state, indicating that the platform has achieved stable levitation.

The 3-DOF responses in vertical, pitch, and roll directions of the platform following initiation levitation are depicted in Fig. 8(a), demonstrating dynamic stabilization after the control system is enabled. After the control loop is enabled, the platform ascends vertically toward the desired air gap. Asynchronous responses of the magnetic units lead to transient tilting in pitch and roll, both of which are progressively compensated by the fractional-order PID feedback control. As described above, the Initiation levitation process entails a high-magnitude step reference input, which serves as a challenging scenario for the maglev control system due to its inherently undamped nature. As a result, under such scenario, integer-order PID controllers typically exhibit significant overshoot and sustain oscillatory behavior.

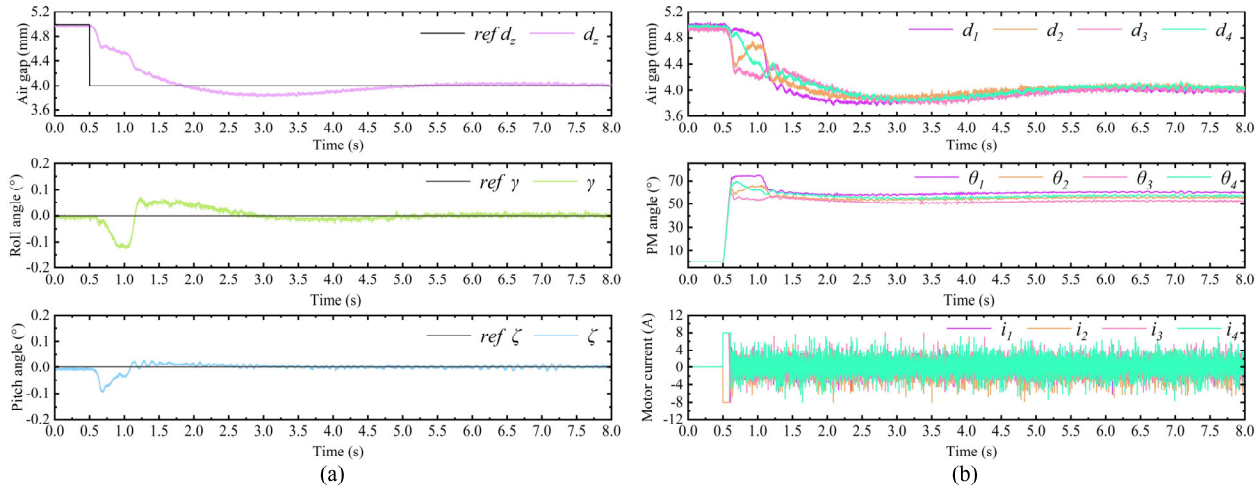

Fig. 8 Experimental results of initiation of the maglev platform

As shown in Fig. 8(a), the vertical response of the platform exhibits a gentle overshoot and slow settling process, which can be attributed to the inherent properties of the FOPID controller. Although dynamic stability is achieved within 1 s after the control is activated, the steady-state error is not fully eliminated until approximately 5 s. Compared to integer PID, the FOPID utilizes non-integer order calculus, which introduces memory and non-local dynamics into the control system. Specifically, the fractional-order integral term accumulates past errors at a slower rate when the integration order is less than one, resulting in a gradual correction process. This helps suppress disturbances but may delay the elimination of steady-state errors. Additionally, the smoother derivative action offered by the fractional-order derivative term

dampens abrupt corrective responses, which contributes to overshoot suppression but reduces responsiveness during recovery. Moreover, the memory effect inherent in fractional-order calculus causes the controller to retain a long-term influence of past error signals, which manifests as a trailing response following a disturbance or step change.

4.3. Levitation experiment during load variation

Subsequently, to further verify the levitation stability of the control system, mass loading application and removal experiments are performed. In the first place, a 500 g mass is added to the geometric center of the levitation platform. After the system stabilizes, the mass is removed. As depicted in Fig. 9(b), the low stiffness of the levitation air gaps results in a rapid expansion of all four magnetic gaps in response to the applied 500g load. To maintain platform levitation, the PM angles are rapidly increased by the servo motors to compensate for the enlarged air gap and additional load. Then, the PM angles are progressively decreased with feedback control. Meanwhile, the four air gaps gradually decreased and reached a steady state. The transient response after the removal of the 500 g load showed an inverse trend in both air gap variations and PM angle adjustments compared to the loading process. However, It should be noted that the magnitude of the instantaneous variation in the air gaps at the moment of unloading was considerably less than that observed during the load application. This phenomenon is attributed to the nonlinear nature of the magnetic force, which is inversely proportional to the square of the air gap. Under identical control parameters, a smaller air gap results in a higher equivalent transient levitation stiffness. Thus, when the mass load is applied in the direction of increasing air gap, the levitation stiffness gradually decreases as the gap enlarges during the response. In contrast, upon load removal, the stiffness increases as the air gap decreases.

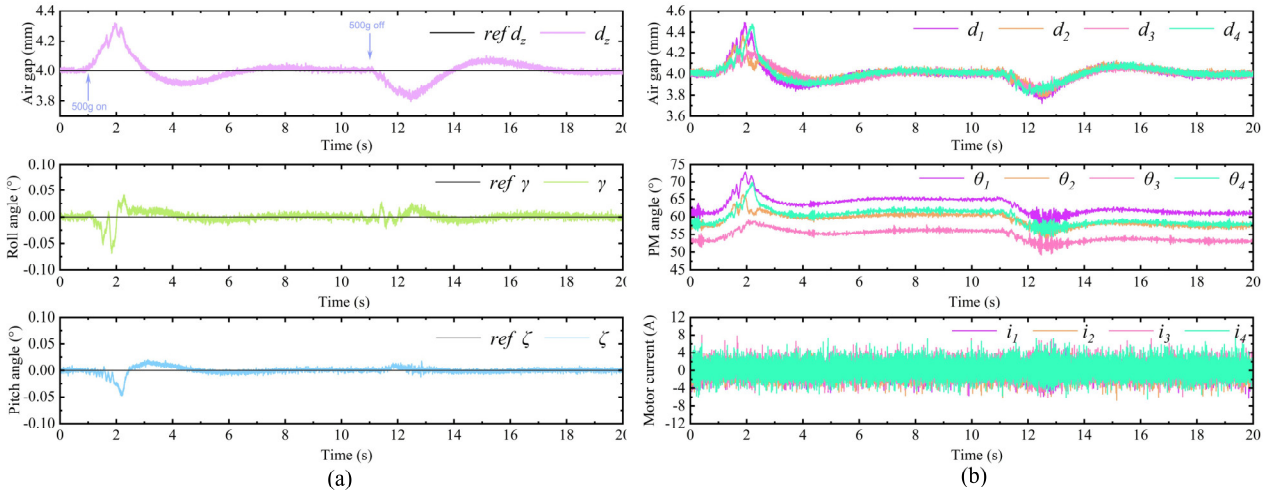

Fig. 9 Experimental verification of platform stability during load variation

Following the application of the external load, the platform experienced transient deviations in its attitude, particularly in the pitch and roll directions, as shown in Fig. 9(a). These fluctuations primarily arose from the response mismatch among the four magnetic units. Nevertheless, the control system effectively mitigated these deviations through the coordinated action of the fractional-order PID controller. Meanwhile, all three degrees of freedom exhibited small overshoots and slow convergence, indicative of the system's inherent underdamped behavior and the moderate responsiveness of the FOPID controller. This response trend, consistent with the levitation initiation process, highlights the trade-off between responsiveness and overshoot suppression under varying load conditions. The gradual return to equilibrium further confirms the system’s ability to sustain stable levitation despite load perturbations.

5. Experiments of fluctuating disturbance suppression

5.1. Fluctuating disturbance suppression with PID control

As described in Sections 4.2 and 4.3, the centralized control system employing a fractional-order PID successfully stabilized the levitation platform. The successful initiation and maintenance of levitation validate the effectiveness of the control strategy. Furthermore, under both mass loading and unloading conditions, the platform exhibited excellent robustness and transient behavior. To further evaluate the external disturbance rejection capability of the levitation

platform, experiments of fluctuating disturbance are conducted. The electromagnetic coil device shown in Fig. 7 is utilized to generate vertical disturbance forces. These disturbances are emulated with a sinusoidal excitation current that simulates the vertical force fluctuations typically produced by linear drive system.

For comparative analysis, the external-loop controller is first configured with the standard PID algorithm to control the 3-DOF of platform. Subsequently, fluctuating disturbance test is carried out under this configuration. As shown in Fig. 10(b), the sinusoidal disturbance current is applied starting at 1 s, with a frequency of 0.5 Hz and an amplitude of 1 A. The disturbance current maintained continuously for a total duration of 29 s, ending at 30 s. Once the sinusoidal current is applied, the four air gaps of units exhibited periodic oscillations due to the alternating vertical attraction force. In the first 10 s after the disturbance was introduced, persistent oscillations were observed in all four air gaps, with their amplitudes progressively attenuated. As for PM angles, they responded rapidly to the air gap fluctuations in order to adjust the magnetic force, thereby ensuring stable levitation of the platform.

As illustrated in Fig. 10, the air gaps showed sustained oscillations throughout the disturbance duration, with only partial attenuation over time. After the initial 10 s, the amplitude reduction plateaued, and fluctuations remained clearly visible. The vertical displacement of the platform closely mirrored this trend. For the roll and pitch axes, the angular displacements are only slightly affected by the vertical disturbance and remained close to 0° throughout the experiment. Compared to the steady-state levitation experiments presented in Section 4, the amplitudes of persistent vibration of the two rotational axes showed a slight increase. The reason for this phenomenon is the higher frequency reciprocating rotation of the PMs induced by internal dynamic coupling, which contributes to the observed residual oscillations.

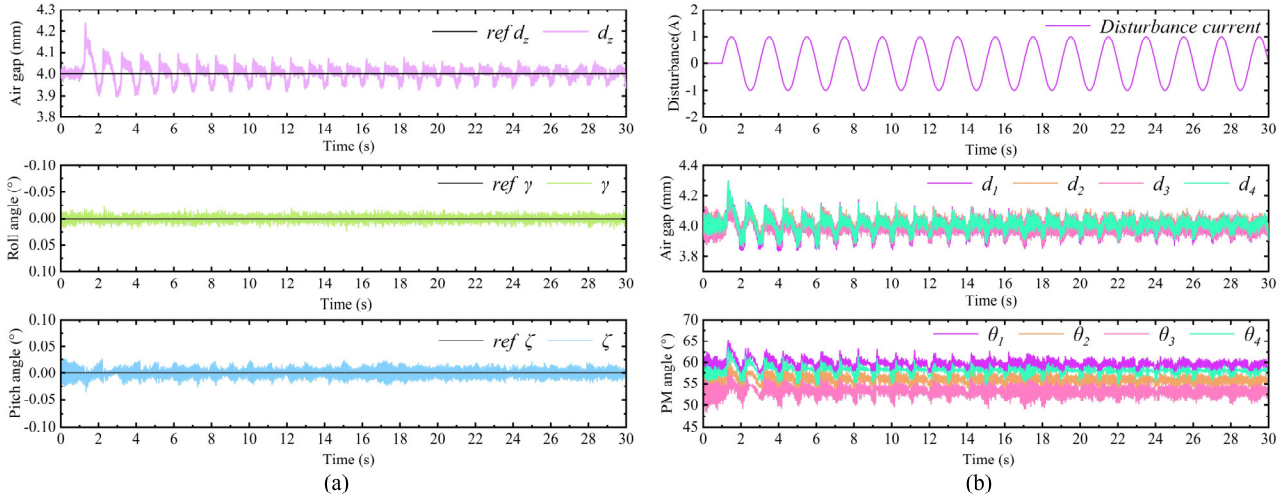

Fig. 10 Experiment of fluctuating disturbance with PID centralized control

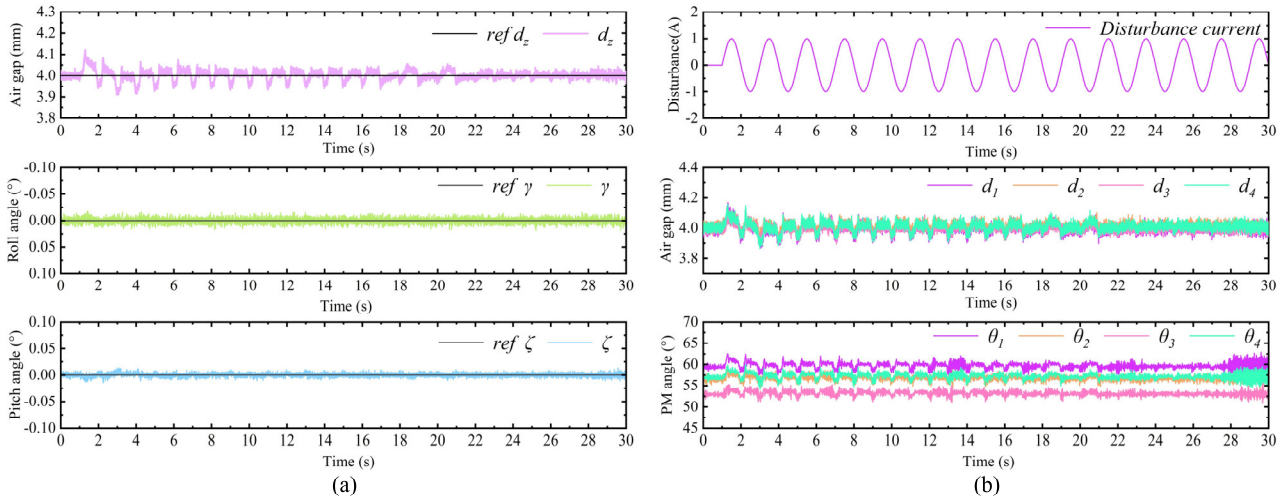

Fig. 11 Experiment of fluctuating external disturbance with FOPID centralized control

5.2. FOPID-Controlled fluctuating disturbance suppression

To further validate the disturbance rejection performance of the fractional-order PID centralized control, the same sinusoidal vertical disturbance current (0.5 Hz, 1 A, applied at 1 s) is introduced under the FOPID-based outer-loop control strategy. The corresponding experimental results are shown in Fig. 11, following the enable of the sinusoidal disturbance current, the air gaps and vertical displacement exhibit transient oscillations which are effectively reduced within approximately 5 s. After an additional 15 s of regulation, the oscillations of all four air gaps are significantly suppressed and nearly eliminated. As for PM angles, they exhibit a much smaller amplitude of reciprocating motion. Consequently, as the platform vibration induced by PM rotation is significantly reduced, the pitch and roll axes of platform exhibited better alignment with their reference positions.

Compared with the PID-controlled results in Fig. 10, the FOPID controller significantly enhanced disturbance attenuation across all observed states. Although the four air gaps were initially disturbed by the sinusoidal excitation, their oscillation amplitudes decayed more rapidly and reached a lower steady-state level. The vertical displacement of the platform followed the reference trajectory more closely, while both pitch and roll angles remained consistently near 0°, exhibiting noticeably reduced jitter. Furthermore, the PM angles responded swiftly and smoothly to compensate for the external excitation, with less aggressive modulation compared to the PID case. These results highlight the FOPID controller's superior ability to regulate magnetic force adaptively, while effectively avoiding the generation of secondary oscillations.

5.3. Analysis and discussion of experimental results

The superior disturbance rejection capability of the fractional-order PID controller stems from its inherent memory effect and frequency-domain flexibility. Unlike standard PID controllers, which rely on fixed integer-order integration and differentiation, FOPID controllers use non-integer orders that allow for gradual and tunable accumulation of error and derivative response. Specifically, the fractional integrator provides smoother low-frequency gain, enabling better suppression of constant or slowly varying disturbances while avoiding excessive phase lag that can destabilize the system. Similarly, the fractional differentiator offers moderate phase lead without amplifying high-frequency noise, contributing to a more balanced control effort. These features allow FOPID controllers to maintain higher loop gain across a broader frequency range, effectively mitigating both low-frequency drift and broadband disturbances.

Moreover, the additional degrees of freedom introduced by the fractional integration and differentiation orders (λ and μ) offer enhanced tuning flexibility to optimize transient response and damping. A lower integration order reduces the aggressiveness of the integral action, minimizing overshoot while still ensuring zero steady-state error. Likewise, a fractional derivative order enables a softer and more controlled response to transient inputs, suppressing oscillations without the noise sensitivity seen in typical derivative terms. This tunability enables FOPID controllers to strike a more effective balance between responsiveness and stability, which is particularly valuable in underdamped systems such as magnetic levitation platforms. In contrast, conventional PID controllers often face trade-offs between fast settling and disturbance rejection, highlighting the practical advantage of FOPID in complex dynamic environments.

6. Conclusion and future work

This paper presented the modeling, control, and experimental validation of a permanent magnet levitation platform using variable flux path magnetic units. A centralized control strategy was developed based on a fractional-order PID controller to address the challenges posed by fluctuating external disturbances. The control strategy ensured stable levitation and robust performance in both initiation levitation and mass variation scenarios, with satisfactory transient characteristics. Compared to the conventional PID controller, under sinusoidal excitations simulating linear motor disturbances, the FOPID controller demonstrated significantly suppresses air gap fluctuations, effectively minimizes platform vibration in all 3-DOF without inducing secondary oscillations. The enhanced control performance is attributed to the memory effect and frequency-domain adaptability of fractional calculus, which allow for better handling of low-frequency and broadband disturbances.

Future research will focus on extending the current control framework to accommodate long-stroke transport applications by integrating the levitation platform with linear motors. Such integration introduces dynamic coupling between the propulsion and vertical axes, where the FOPID centralized strategy is expected to play a key role in maintaining system stability, ensuring precise coordination and robust decoupling.

Acknowledgments

This work was supported by the National Natural Science Foundation of China (Grant No. 52405284, 52375258), the National R&D Program of China (Grant No. 2024YFB3410002), the Natural Science Foundation of Liaoning Province, China (Grant No. 2023-BSBA-263), and Scientific Research Fund Project of Liaoning Provincial Department of Education (Grant No. JYTMS20231191, LJ222410142008, and LJ212410142015). Support from the China Postdoctoral Science Foundation (Grant No. 2024M762160) is also gratefully acknowledged.

References

Chopade, A.S., Khubalkar, S.W., Junghare, A.S., Aware, M.V., Das, S., 2018. Design and implementation of digital fractional order PID controller using optimal pole-zero approximation method for magnetic levitation system. IEEE/CAA Journal of Automatica Sinica 5, 977989. https://doi.org/10.1109/JAS.2016.7510181

Duan, J., Zhou, H., Guo, N., 2011. Electromagnetic Design of a Novel Linear Maglev Transportation Platform With Finite-Element Analysis. IEEE Transactions on Magnetics 47, 260263. https://doi.org/10.1109/tmag.2010.2087388

Feng, Y., Zhao, C., Peng, Y., Zhang, W., Yu, D., Liang, X., 2025. Influence of levitation bogie structure aerodynamic loads on the dynamic performance of 600 km/h EMS maglev train. Journal of Wind Engineering and Industrial Aerodynamics 261, 106070. https://doi.org/10.1016/j.jweia.2025.106070

Ha, C.-W., Kim, C.-H., Lim, J., 2018. Experimental Verification of a Magnetic Levitation Transport System for the OLED Display Evaporation Process Under Vacuum. IEEE Robotics and Automation Letters 3, 27862791. https://doi.org/10.1109/lra.2018.2839199

Hu, K., Xu, J., Ai, Y., Rong, L., Lin, G., Yuan, Y., 2024. Super-Twisting-Observer-Based Equivalent-Input-Disturbance Compensation Suspension Control of Medium-Low Speed Maglev. IEEE Transactions on Vehicular Technology 73, 90099014. https://doi.org/10.1109/TVT.2024.3355110

Kim, E.K., Jung, J.W., Yoon, H.M., Yoon, J.Y., 2024. Near-Zero-Power 2-DOF Noncontact Transportation by Static and Dynamic Disturbance Compensation Using Single-Body PM-Biased Magnetic Levitator. IEEE/ASME Trans. Mechatron. 29, 767776. https://doi.org/10.1109/TMECH.2023.3291725

Kim, J., Ha, C.W., King, G.B., Kim, C.H., 2020. Experimental development of levitation control for a high-accuracy magnetic levitation transport system. ISA Trans 101, 358365. https://doi.org/10.1016/j.isatra.2020.01.026

Kim, K.-J., Han, H.-S., Kim, C.-H., Yang, S.-J., 2013. Dynamic Analysis of a Maglev Conveyor Using an EM-PM Hybrid Magnet. Journal of Electrical Engineering and Technology 8, 15711578. https://doi.org/10.5370/jeet.2013.8.6.1571

Maslen, E.H., Schweitzer, G. (Eds.), 2009. Magnetic Bearings: Theory, Design, and Application to Rotating Machinery. Springer, Berlin, Heidelberg. https://doi.org/10.1007/978-3-642-00497-1

Song, C., Zhou, Z., Xie, S., Hu, Y., Zhang, J., Wu, H., 2015. Fuzzy control of a semi-active multiple degree-of-freedom vibration isolation system. Journal of Vibration and Control 21, 16081621. https://doi.org/10.1177/1077546313480997

Sun, F., Oka, K., Saibara, Y., 2010. Magnetic suspension system by flux path control using rotary actuator. International Journal of Applied Electromagnetics and Mechanics 33, 769776. https://doi.org/10.3233/jae-2010-1184

Sun, F., Pei, W., Zhao, C., Jin, J., Xu, F., Zhang, X., 2022. Permanent Maglev Platform Using a Variable Flux Path Mechanism: Stable Levitation and Motion Control. IEEE Transactions on Magnetics 58, 110. https://doi.org/10.1109/tmag.2022.3174452

Swethamarai, P., and Lakshmi, P., 2022. Adaptive-Fuzzy Fractional Order PID Controller-Based Active Suspension for Vibration Control. IETE Journal of Research 68, 34873502. https://doi.org/10.1080/03772063.2020.1768906

Wang, Y., Zhang, S., Guo, H., Tian, X., Wu, Z., 2025. Intelligent tuning of fractional-order PID control for performance optimization in active suspension systems. Journal of Vibration and Control 10775463251348002. https://doi.org/10.1177/10775463251348002

Wu, H., Zhou, J., Xie, C., Zhang, J., Huang, Y., 2021. Two-dimensional time series sample entropy algorithm: Applications to rotor axis orbit feature identification. Mechanical Systems and Signal Processing 147, 107123. https://doi.org/10.1016/j.ymssp.2020.107123

Wu, Q., Liu, Z., An, F., Liu, B., 2025. Self-tuning PID feedback control method for magnetic suspension active vibration isolation system with parameters uncertainty. Journal of Vibration and Control 31, 431443. https://doi.org/10.1177/10775463241228018

Xu, C., Sun, F., Zhang, X., Jin, J., Xu, F., Zhao, C., Lu, W., Wang, Y., Ji, Z., Zheng, H., 2025. A 1-DOF Controlled Full

Levitation Hybrid Magnetic Bearing for Compact Centrifugal Kidney Pumps. IEEE Transactions on Magnetics 61, 114. https://doi.org/10.1109/TMAG.2025.3558664
Zhao, C., Oka, K., Sun, F., Harada, A., Jin, J., Zhang, M., 2022a. Design of Zero-Power Control Strategy With Resisting Tilt of Hybrid Magnetic Levitation System. IEEE Transactions on Industrial Electronics 69, 1139411402. https://doi.org/10.1109/tie.2021.3121670
Zhao, C., Sun, F., Jin, J., Pei, W., Xu, F., Oka, K., Zhang, M., 2022b. Research of permanent magnetic levitation system: Analysis, control strategy design, and experiment. Proceedings of the Institution of Mechanical Engineers, Part C: Journal of Mechanical Engineering Science 236, 76177628. https://doi.org/10.1177/09544062221078199
Zhao, C., Sun, F., Jin, J., Tang, H.J., Xu, F., Li, Q., Oka, K., 2020. Analysis of Quasi-Zero Power Characteristic for a Permanent Magnetic Levitation System with a Variable Flux Path Control Mechanism. IEEE/ASME Transactions on Mechatronics 26, 11. https://doi.org/10.1109/tmech.2020.3026086
Zhou, H., Deng, H., Duan, J., 2018. Hybrid Fuzzy Decoupling Control for a Precision Maglev Motion System. IEEE/ASME Transactions on Mechatronics 23, 389401. https://doi.org/10.1109/tmech.2017.2771340
Zhou, L., Trumper, D.L., 2021. Magnetically Levitated Linear Stage With Linear Bearingless Slice Hysteresis Motors. IEEE/ASME Transactions on Mechatronics 26, 10841094. https://doi.org/10.1109/TMECH.2020.3017435